BL11XU
QST Quantum Dynamics I

1. Introduction

BL11XU is an in-vacuum undulator beamline operated by the National Institutes for Quantum Science and Technology (QST). It is designed to provide scientists and engineers with a wide range of options on advanced synchrotron radiation and quantum functional material research. In BL11XU, switchable Si(111) and Si(311) double-crystal monochromators cooled by liquid nitrogen are installed in the optical hutch. Highly brilliant and well-collimated synchrotron X-rays are available in the energy range of 6–70 keV. There are three experimental hutches; each one contains specialized measurement instruments for studies using Mössbauer spectroscopy (EH1), inelastic X-ray scattering and X-ray magnetic circularly polarized emission (EH2), and surface X-ray diffraction (EH3).

2.Mössbauer spectroscopy

Thermal diffuse scattering (TDS) diffraction from a crystal is a fascinating research subject [1]. However, the angular resolution of γ-ray diffraction with a traditional ^{57}Co source is limited, and thus it has been impossible to observe the dynamical effects in TDS diffraction at the Bragg angle of a perfect crystal requiring an angular resolution of less than 1". In contrast, synchrotron Mössbauersource (SMS) γ-rays have an energy bandwidth of ~10^{-8} eV and the angular divergence of ~3.0 arcseconds. If an asymmetric Si reflection collimator is used together, γ-rays with a low angular divergence of 1" or less can be obtained. Recently, the dynamical effects on the TDS reflection at the Si 111 Bragg angle have been observed for the first time using a SMS and a resonant absorber [2].

The optical setup is shown in Fig. 1. The SMS ($^{57}FeBO_3$(111)) emitted π-polarized Mössbauer γ-rays. A symmetric Si(111) was used for the first crystal and the vertical beam divergence was collimated to ω_{in}~0.6", whose value was smaller than the FWHM (ω_T ~ 3.6") of the rocking curve (RC) of the second crystal (symmetric Si(111)). After the first crystal, the energy bandwidth of the γ-rays was 1.6×10^{-8} eV, and the Si(111) reflection intensity was counted by the NaI(Tl) detector.

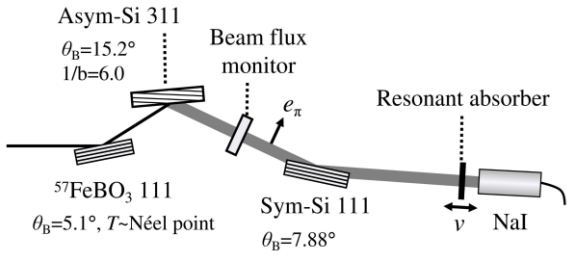

Fig. 1. Optical setup for Mössbauer diffraction.

To determine the elastic $I_{el}(2\theta)$ and inelastic $I_{in}(2\theta)$ scattering intensities at the Bragg peak, the Si 111 diffraction intensities $I_R(2\theta)$ and $I_\infty(2\theta)$ were measured through a resonant absorber, where $I_R(2\theta)$ and $I_\infty(2\theta)$ are the intensities of the γ-rays scattered at the angle 2θ with the resonant absorber under on- and off-resonance conditions, respectively. ^{57}Fe-enriched ammonium lithium fluoroferrate (ALF) was used as the resonant absorber, whose resonance linewidth was ~1.0×10^{-7} eV, which is much larger than that of the SMS γ-rays: the ALF at rest can act as a mask absorber for

the elastic component of the γ-rays diffracted by the second crystal. First, $I_R(2\theta)$ was measured using the resonant absorber at rest (on-resonance). Then, $I_\infty(2\theta)$ was measured by oscillating the resonant absorber in the sinusoidal velocity mode at 10 Hz and a maximum velocity of 20 mm/s, breaking the resonance condition (off-resonance). In this case, the elastic and inelastic scattering intensities $I_{el}(2\theta)$ and $I_{in}(2\theta)$ are obtained from the following equations: $I_{el}(2\theta)=(I_\infty(2\theta)-I_R(2\theta))/P_0$, $P_0=(I_\infty(0)-I_R(0))/I_\infty(0)$, and $I_{in}(2\theta)=I_\infty(2\theta)-I_{el}(2\theta)$, where the constant P_0 is obtained by on- and off-resonance measurements on the direct beam without a second crystal. P_0 was 0.80, which was measured with the detector placed in the forward direction.

Figure 2 shows the experimental results, which correspond to I_{el} (RC) and I_{in}(TDS diffraction curve) on the Si 111 reflection. For comparison, Fig. 2 also shows the calculated RC and extinction distance (ED) of Si(111) reflection for π-polarized 14.4keV γ-rays.

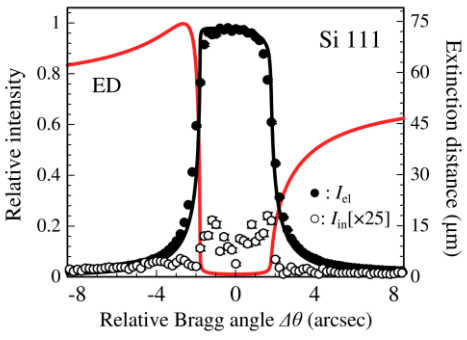

Fig. 2. Elastic (RC) and inelastic (TDS) components of Si 111 Bragg reflection.

The RC shows a well-known asymmetric profile. On the other hand, the TDS diffraction shows an intensity anomaly based on dynamical effects. At $|\Delta\theta| < 1.8"$, it is seen that the TDS increases under Bragg conditions, but that at the angle ($\Delta\theta = 0$), the ED reaches a minimum. This behavior is due to a decrease in the effective volume of the crystal contributing to the TDS [1]. A unique feature is that the TDS is slightly larger on the RC high angle shoulder ($\Delta\theta = 1.8"$) than on the RC low angle shoulder ($\Delta\theta = -1.8"$), despite having almost the same ED value. This suggests that, for the wave field having the antinode at the atomic planes, the cross sections of TDS diffraction are relatively larger than those for the wave field having the node at the atomic planes. In the angular region away from the Bragg peak ($|\Delta\theta| > 4"$), it is seen that the TDS is larger at lower angles ($\Delta\theta < -4"$) than at higher angles ($\Delta\theta > 4"$). For now, we speculate that this is simply due to the volume effect in the TDS: in these angular regions, the influence of a standing wave formed in the crystal is weakened, while the penetration depth is much larger at lower angles than at higher angles. The results confirmed that the SMS enabled the study of the dynamical effects on the TDS of a Si crystal at a high energy resolution of 10^{-7} eV order and a high angular resolution below 1.0".

3. Inelastic X-ray scattering

An inelastic X-ray scattering spectrometer for hard X-rays installed in EH2 is used for resonant inelastic X-ray scattering (RIXS) at the K-edge of the 3*d* transition metals and the L-edge of the 5*d* transition metals. The optics of EH2 provides an energy resolution of 0.1–1 eV for both incident and scattered (emitted) X-rays. High-energy-resolution fluorescence-detected X-ray absorption spectroscopy (HERFD-XAS) is also available using the spectrometer.

Two pairs of Si(111) and Si(311) crystals

are mounted in the double-crystal monochromator (DCM) in BL11XU. The Si(311) DCM was originally designed for high-energy X-rays above 35 keV, but it is also used as a monochromator with higher energy resolution than that of Si(111) at around 10 keV. We tested the Si(311) DCM for HERFD-XAS experiments at the Pt L_3-edge and confirmed that it gives comparable performance to standard optics with a combination of the Si(111) DCM and a Si(400) channel-cut crystal monochromator (CCM). The advantage of the Si(311) DCM is its simpler alignment procedure; for example, we do not have to worry about the energy mismatch between DCM and CCM during the experiment. The typical parameters for the two types of optics are summarized in Table1. Even though a longer scan time is necessary for the Si(311) DCM owing to the larger rotation angle for a certain energy step, it can be compensated by the higher intensity. A slight difference in energy resolution is negligible for the HERFD-XAS experiment.

X-ray emission spectroscopy is another technique using the spectrometer in EH2. Brilliant synchrotron radiation enables one to measure the X-ray emission produced by a transition from a valence state to a core level, which is much weaker in intensity than the transition between core levels, and it has recently been developed as a new X-ray spectroscopy technique named valence-to-core X-ray emission spectroscopy (VtoC XES). It has a great potential to measure valence electronic states under operando conditions. We have started the VtoC XES experiments at EH2. As a first step, we measured the systematic doping dependence of superconducting cuprates and evaluated the sensitivity of VtoC XES to the carrier density in the valence orbitals.

Table 1. Comparison of the two types of incident X-ray optics for HERFD-XAS at the Pt L_3-edge. Intensity and scan time are normalized to the value of DCM Si(111)+Si(400) CCM. The scan time is measured for the 25 eV range divided into 50 steps.

optics	scan time	intensity	energy resolution
Si(111) DCM + Si(400) CCM	1	1	380 meV
Si(311) DCM	1.12	1.21	460 meV

4. X-ray magnetic circularly polarized emission

X-ray magnetic circularly polarized emission (XMCPE) is a phenomenon in which characteristic X-rays emitted from a magnetized material are circularly polarized, which has been reported very recently as a new magneto-optical effect in the X-ray region [3]. An advantage of XMCPE is the large flipping ratio (~25%) in the hard X-ray region for 3*d* transition metal elements. This feature is well suited for observations of magnetic microstructures well below the sample surface.

The development of a bulk-sensitive magnetic microscope utilizing XMCPE started in FY2018 at BL11XU, and a scanning X-ray magnetic microscope with a lateral resolution of 10 μm was successfully constructed in FY2020 [4]. A schematic illustration of the microscope is shown in Fig. 3. With this microscope, magnetic domains in grain-oriented electrical steel have been

investigated. In FY2019 and FY2020, in parallel with the development of the microscope, (i) two-dimensional magnetic domain images of supplementary domains were measured at several different exit angles to unveil the magnetic domain structure and (ii) two-dimensional images of magnetic domains in a domain-refined grain-oriented electrical steel sheet were measured at several applied magnetic fields to examine the magnetization reversal process.

In FY2021, we continued the development of the three-dimensional visualization of magnetic domains. A major technical problem is the large acceptance volume of the collimating mirror. By employing two analyzer crystals with a ++ arrangement, we proved that the acceptance volume can be reduced, and we succeeded in obtaining several depth-resolved profiles of magnetic domains.

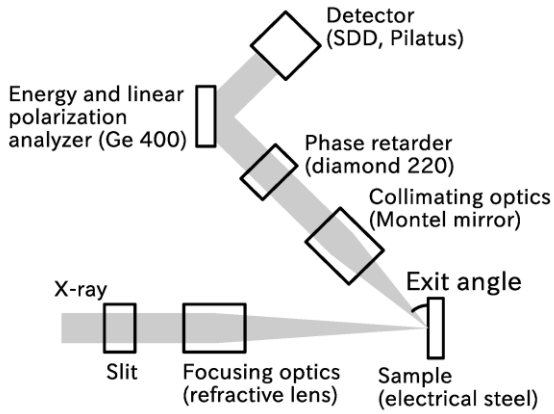

Fig. 3. Schematic of XMCPE microscope in BL11XU.

5. Surface X-ray diffraction

EH3 is equipped with a surface X-ray diffractometer connected with a molecular beam epitaxy (MBE) chamber [5,6]. This instrument is designed for *in situ* studies on III–V group semiconductor surfaces, especially surface crystallography under MBE conditions and growth dynamics of multilayer and nanostructures. III–V group semiconductors are nitrides such as GaN and InN and arsenides such as GaAs and InAs. These semiconductors are grown by exchanging two types of MBE chamber.

Our recent activity on nitrides focuses on the initial stages of GaN growth on graphene-covered SiO_2 substrates because graphene weakly interacts with the substrate and grown materials. GaN growth on graphene allows us to produce free-standing GaN films by mechanical exfoliation, which can contribute to flexible photonics/electronics applications [7]. We compared the initial growth characteristics of GaN with or without AlN buffer grown on the graphene-covered SiO_2 substrates by *in situ* X-ray diffraction. When the AlN buffer layers were deposited before GaN growth, the lattice parameters of both AlN and GaN changed during GaN growth, indicating that AlN acts as a seed for GaN growth. Furthermore, GaN preferred to have an epitaxial relationship with graphene, demonstrating that even monolayer graphene can be a template for GaN growth. We also confirmed that GaN on graphene can be exfoliated mechanically. GaN growth on graphene-covered SiO_2 can lead to the fabrication of free-standing GaN films by mechanical exfoliation and will be useful for flexible devices.

Mitsui Takaya[*1], Ishii Kenji[*1], Inami Toshiya[*1], and Sasaki Takuo[*2]

[*1] Magnetism Research Group, Synchrotron Radiation Research Center,National Institutes for Quantum Science and Technology

[*2] Coherent X-ray Research Group, Synchrotron

Radiation Research Center, National Institutes for Quantum Science and Technology

References:

[1] O'Connor, D. A. & Butt, N. M. (1963). *Phys. Lett.* **7**, 233.

[2] Mitsui, T. Fujiwara, K. Imai, Y. & Yoda, Y. (2022). *J. Phys. Soc. Jpn.* **91**, 035002.

[3] Inami, T. (2017). *Phys. Rev. Lett.***119**, 137203.

[4] Sugawara, K. Inami, T. Nakada, T. Sakaguchi, Y. & Takahashi, S. (2021). *J. Appl. Phys.***130**, 113901.

[5] Takahasi, M. (2013). *J. Phys. Soc. Jpn*. **82**, 021011.

[6] Sasaki, T. et al. (2016). *Jpn.J. Appl. Phys.* **55**, 05FB05.

[7] Fuke, S. et al. (2020).*Jpn.J. Appl. Phys.***59**, 070902.